

Article

Ce-Doped Three-Dimensional Ni/Fe LDH Composite as a Sulfur Host for Lithium–Sulfur Batteries

Huiying Wei, Qicheng Li, Bo Jin * and Hui Liu

Key Laboratory of Automobile Materials, Ministry of Education, and School of Materials Science and Engineering, Jilin University, Changchun 130022, China; weihy22@mails.jlu.edu.cn (H.W.); liqc20@mails.jlu.edu.cn (Q.L.); liuhui20@mails.jlu.edu.cn (H.L.)

* Correspondence: jinbo@jlu.edu.cn

Abstract: Lithium–sulfur batteries (LSBs) have become the most promising choice in the new generation of energy storage/conversion equipment due to their high theoretical capacity of 1675 mAh g^{-1} and theoretical energy density of 2600 Wh kg^{-1} . Nevertheless, the continuous shuttling of lithium polysulfides (LiPSs) restricts the commercial application of LSBs. The appearance of layered double hydroxides (LDH) plays a certain role in the anchoring of LiPSs, but its unsatisfactory electronic conductivity and poor active sites hinder its realization as a sulfur host for high-performance LSBs. In this paper, metal organic framework-derived and Ce ion-doped LDH (Ce-Ni/Fe LDH) with a hollow capsule configuration is designed rationally. The hollow structure of Ce-Ni/Fe LDH contains a sufficient amount of sulfur. Fe, Ni, and Ce metal ions effectively trap LiPSs; speed up the conversion of LiPSs; and firmly anchor LiPSs, thus effectively inhibiting the shuttle of LiPSs. The electrochemical testing results demonstrate that a lithium–sulfur battery with capsule-type S@Ce-Ni/Fe LDH delivers the initial discharge capacities of 1207 mAh g^{-1} at 0.1 C and 1056 mAh g^{-1} at 0.2 C, respectively. Even at 1 C, a lithium–sulfur battery with S@Ce-Ni/Fe LDH can also cycle 1000 times. This work provides new ideas to enhance the electrochemical properties of LSBs by constructing a hollow capsule configuration.

Keywords: lithium–sulfur batteries; layered double hydroxide; hollow capsule; shuttling effect; lithium polysulfides



Citation: Wei, H.; Li, Q.; Jin, B.; Liu, H. Ce-Doped Three-Dimensional Ni/Fe LDH Composite as a Sulfur Host for Lithium–Sulfur Batteries. *Nanomaterials* **2023**, *13*, 2244. <https://doi.org/10.3390/nano13152244>

Academic Editor: Henrich Frielinghaus

Received: 29 June 2023

Revised: 28 July 2023

Accepted: 1 August 2023

Published: 3 August 2023



Copyright: © 2023 by the authors. Licensee MDPI, Basel, Switzerland. This article is an open access article distributed under the terms and conditions of the Creative Commons Attribution (CC BY) license (<https://creativecommons.org/licenses/by/4.0/>).

1. Introduction

With the sustainable development of the economy and society, people’s sense of crisis about fossil fuel exhaustion is increasing day by day. It has become an inevitable trend of future development to abandon our dependence on resources and develop advanced electrochemical energy storage/conversion systems. Lithium–sulfur batteries (LSBs) have been extensively studied by researchers due to their high theoretical capacity and theoretical energy density (Table S1) [1,2]. Although LSBs possess broad prospects, they often encounter many troubles in practical applications, such as the poor electronic conductivity of active sulfur, the shuttling effect of lithium polysulfides (LiPSs), and the volumetric expansion of cathode materials during the charging/discharging processes.

To solve these problems, people have invested a lot of energy into the research and development of cathode materials in the past decades. So far, there are massive sulfur host materials, such as carbonaceous materials [3,4], metal compounds [5–12], and so on. Metal organic frameworks (MOFs) materials are excellent templates to synthesize hollow polyhedrons and hollow carbon materials by means of calcining or etching [13,14]. In recent years, layered double hydroxide (LDH) has been proven to adsorb LiPSs effectively in LSBs [15–17] and is also used in supercapacitors [18,19]. Due to sufficient hydrophilic points and hydroxyl groups [15], LiPSs are not easily dissolved in organic electrolytes, thus promoting the redox kinetics of LiPSs. A novel lithium–sulfur battery configuration

was designed by Hwang et al. [15], which consists of a sulfur and magnesium–aluminum-layered double hydroxide (MgAl LDH) carbon nanotube composite material as the positive electrode and a modified separator. This configuration achieves high specific capacity and good capacity retention, and this positive electrode can be used for both the catalytic conversion of LiPSs and anchoring of LiPSs, thereby improving the rapid reaction kinetics and Coulombic efficiency (CE). Chen et al. [16] used ZIF-67 as a template to prepare a regular nanocapsid-shaped NiCo-LDH/Co₉S₈ (H-LDH/Co₉S₈) hollow structure to inhibit LiPS diffusion, and its hollow structure accommodates sufficient sulfur. Rich O and Co sites block the migration and diffusion of LiPSs through chemical bonding and promote the transformation kinetics of LiPSs. At 0.1 C, H-LDH/Co₉S₈ has a high initial capacity of 1339.1 mAh g⁻¹. H-LDH/Co₉S₈ possesses an ultra-long lifespan of up to 1500 cycles (0.047% of the capacity decay rate per cycle, 1 C) and a stable CE of over 98%. This work opens up a new way for LDH materials to be used as sulfur carrier materials for high-performance LSBs. Zhang et al. [17] designed and synthesized nanocages with two shells of Co(OH)₂ and layered double hydroxides (CH@LDHs) as a new sulfur carrier for LSBs. The CH@LDH/S composite delivers a satisfactory first discharge capacity (1014 mAh g⁻¹, 0.1 C) and still remains at 653 mAh g⁻¹ after 100 cycles. In addition, at 0.5 C, the first discharge capacity is 747 mAh g⁻¹, and this specific capacity slowly decays to 491 mAh g⁻¹ after 100 cycles. The above results demonstrate that the CH@LDH matrix successfully inhibits the diffusion of LiPSs.

Inspired by the above works, we combined MOF with LDH to design a MOF-derived LDH material with regular three-dimensional (3D) spatial configuration to be used as an ideal sulfur host for high-performance LSBs. Firstly, MIL-88A is used as a template [20], and Ce and Ni ions are added into the alkaline solution for etching. Ce ion doping makes the coordination environment of the MIL-88A polyhedron more stable, especially in the weakly alkaline solution. While the reaction is in progress, urea produces more OH⁻, damaging the MIL-88A polyhedron. With the sustainable precipitation of Ni, Fe, and Ce ions, interconnected nanosheets are formed outside the MIL-88A precursor. Finally, a hollow Ce-Ni/Fe LDH capsule is obtained. The unique structure of Ce-Ni/Fe LDH not only provides the space for the volumetric expansion of the cathode material upon cycling but also supplies abundant polar metal sites to anchor LiPSs and promote the transformation of LiPSs. The electrochemical testing results demonstrate that a lithium–sulfur battery with S@Ce-Ni/Fe LDH delivers the first discharge capacities of 1207 mAh g⁻¹ at 0.1 C and 1056 mAh g⁻¹ at 0.2 C, respectively. After a long cycle, a satisfactory discharge capacity and an average capacity decay rate per cycle are also achieved (940 mAh g⁻¹, 0.067% for 1000 cycles) at 1 C (based on the second cycle).

2. Materials and Methods

2.1. Synthesis of MIL-88A Polyhedron

Ferric chloride hexahydrate (1.35 g) and fumaric acid (0.58 g) were dissolved in 50 mL deionized (DI) water, respectively. The solution of ferric chloride hexahydrate was quickly added to the solution containing fumaric acid and then poured into a round-bottomed flask and placed in an oil bath at 100 °C for 4 h. At last, the red-brown product was collected and washed with DI water and ethanol, respectively.

2.2. Synthesis of Ni/Fe LDH Polyhedron

The obtained precursor (27.5 mg) was ultrasonically dispersed in ethanol (4 mL), and Ni(NO₃)₂·6H₂O (150 mg) and urea (100 mg) were dissolved in DI water (6 mL). Then, two solutions were evenly mixed and sealed in a round-bottomed flask, bathed in an oil bath, and continuously heated at 90 °C for 5 h. During this process, the OH⁻ ions produced by urea hydrolysis gradually corroded the MIL-88A template. The released Fe³⁺, Ni²⁺, and OH⁻ ions were coprecipitated to form a thin shell. The hollow Ni/Fe LDH polyhedron product was rinsed with ethanol and DI water 3 times, respectively, and dried for 12 h at 60 °C.

2.3. Synthesis of Ce-Ni/Fe LDH Capsule

The prepared MIL-88A (27.5 mg) was ultrasonically dispersed in ethanol (4 mL). $\text{Ni}(\text{NO}_3)_2 \cdot 6\text{H}_2\text{O}$ (142.5 mg), $\text{Ce}(\text{NO}_3)_3 \cdot 6\text{H}_2\text{O}$ (7.5 mg), and urea (100 mg) were dissolved in DI water (6 mL). Two solutions were evenly mixed and stirred to obtain a new solution. The new solution was placed in a Teflon-lined reactor and continuously reacted at 120 °C for 5 h. The resulting product was rinsed with ethanol and DI water, respectively, and dried overnight at 60 °C to obtain a 3D hollow Ce-Ni/Fe LDH capsule.

2.4. Synthesis of S@Ce-Ni/Fe LDH

Ce-Ni/Fe LDH and sublimated sulfur were mixed and ground thoroughly in accordance with the mass ratio of 1:3. The mixture was heated for 12 h at 155 °C under Ar atmosphere. After being cooled to room temperature, the S@Ce-Ni/Fe LDH composite was collected. For comparison, the S@Ni/Fe LDH composite was also prepared by the same method, as shown in Figure 1.

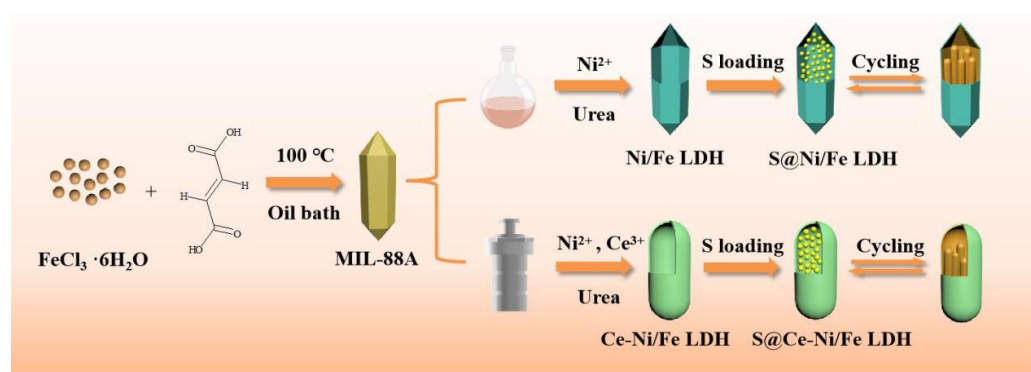


Figure 1. Schematic diagram of the synthesis of S@Ni/Fe LDH and S@Ce-Ni/Fe LDH.

2.5. Preparation of Li_2S_6 Solution

To test the adsorption capacity of the materials for the LPSs, the Li_2S_6 (5 mM) solution was synthesized. S and Li_2S (5:1, molar ratio) were added to a mixture of 1,3-dioxolane (DOL) and 1,2-dimethoxymethane (DME). At Ar atmosphere, the solution was stirred for 12 h at 60 °C to obtain the Li_2S_6 solution.

2.6. Materials Characterization

The crystal structures were analyzed by a D/Max-2500/PC X-ray diffractometer (XRD). The morphologies were characterized by JSM-6700F scanning electron microscopy (SEM), field emission SEM (FESEM), scanning transmission electron microscopy (STEM), JEM-2100F transmission electron microscopy (TEM), and high-resolution TEM (HRTEM). The valence states and elements were analyzed by a ESCALAB-250Xi X-ray photoelectron spectrometer. The thermogravimetric test (TGA) was carried out with a NETZSCH STA 499 F3 device. UV–Vis absorption spectra of the adsorbed Li_2S_6 solutions were measured by an Evolution 300 UV–Vis spectrophotometer. The N_2 adsorption/desorption test by a Micromeritics ASAP 2020 analyzer was performed to measure the pore size distribution and specific surface area at 77 K. The pore size distribution and specific surface area were measured by the Barrett–Joyner–Halenda (BJH) method. The wetting angles were determined by the OCA25 contact angle measuring instrument. The molar ratio of the Ni, Fe, and Ce ions in the Ce-Ni/Fe LDH composite was analyzed with an inductive coupled plasma spectrometer.

2.7. Electrochemical Measurements

S@Ce-Ni/Fe LDH, acetylene black, and polyvinylidene fluoride were fully ground according to the mass ratio of 70:20:10 and mixed with a N-methyl pyrrolidinone solvent to prepare an electrode slurry, which was evenly coated on Al foil and then dried for 12 h

at 60 °C in a vacuum oven to construct the electrode sheet. For comparison, S@Ni/Fe LDH and pure sulfur electrodes were also prepared using the same method. The active sulfur loading in the cathode was approximately 1.0 mg cm⁻². CR2025 button-type LSBs were assembled in a glovebox filled with an argon atmosphere using different electrodes (S@Ce-Ni/Fe LDH, S@Ni/Fe LDH, and pure S) as the cathode; lithium as the anode; and polypropylene (PP) as the separator. LiTFSI (1 M) in a mixture solvent of DOL and DME (1:1, volume) with 2 wt% LiNO₃ was utilized as the electrolyte. The cycle performance and rate performance of the assembled LSBs were tested using a charge/discharge tester (LAND CT2001A) with a voltage interval of 1.7–2.8 V (1 C = 1675 mA g⁻¹). The reversible capacities of the batteries were calculated according to the weight of active sulfur. Cyclic voltammetry (CV) and electrochemical impedance spectroscopy (EIS) tests were performed at an electrochemical workstation (CHI650D). In the CV, the scan rate was 0.1 mV s⁻¹. The voltage in the EIS was 5 mV, and the frequency range was 0.01–10⁶ Hz.

3. Results and Discussion

Figure 2a and Figure S1a,b show FESEM images of the MIL-88A precursor. The length and width of the as-synthesized MIL-88A precursor are approximately 4–5 and 1 μm, respectively. It is obvious that the morphology and particle size of the as-synthesized MIL-88A precursor are uniform. Figures 2b and S2a,b display FESEM images of Ce-Ni/Fe LDH. It is seen that the MIL-88A precursor transforms from a polyhedron into a capsule structure with 3D alternately connected layers during the reaction process. Ce ion has excellent polyvalency, agile coordination, and a great affinity for oxygen-containing donors. The growth process can be effectively regulated by introducing a Ce ion-doping form rather than an interface structure form. The crystallographic stability, morphology, and performance of the as-obtained crystals can be optimized [21]. Figure 2c shows the FESEM image of S@Ce-Ni/Fe LDH, which maintains the same morphology and structure as Ce-Ni/Fe LDH. There is sulfur filling in the lamellar shell gap, but more sulfur is integrated into its capsule interior. Thus, this structure has enough space to hold sulfur and effectively alleviates the volumetric change during cycling. At the same time, this structure possesses a large amount of exposed active sites to anchor LiPSs, thus limiting their dissolution and diffusion [22,23]; that is to say, a large number of exposed active surfaces and metal active sites can absorb LiPSs effectively, which provides a strong obstacle to the dissolution and diffusion of LiPSs during charging/discharging processes [24,25]. Figures 2d,e and S2c,d display TEM images of Ce-Ni/Fe LDH. It can be seen that the capsule-like Ce-Ni/Fe LDH shell is composed of lamellated Ce-Ni/Fe LDH, and the inside is a hollow structure. Figure 2f shows a HRTEM image in which a lattice fringe of 0.262 nm corresponds to the (012) crystal plane of Ce-Ni/Fe LDH. In Figure 2g–k, the presence of the Ce, Ni, Fe, and O elements and their spatially homogeneous distribution in the Ce-Ni/Fe LDH capsule are clearly observed. Comparing SEM image of Ni/Fe LDH with the corresponding element mapping results (Figure S3), it is observed that Ce ions have been successfully doped in Ce-Ni/Fe LDH and uniformly distributed in the Ce-Ni/Fe LDH capsule. In Figure S4, it is obvious that the S, Ce, Fe, Ni, and O elements are evenly distributed in S@Ce-Ni/Fe LDH.

Figure 3a shows the XRD patterns of Ni/Fe LDH, Ce-Ni/Fe LDH, and S@Ce-Ni/Fe LDH, and the XRD pattern of the MIL-88A precursor is displayed in Figure S1c. The characteristic peaks of the as-synthesized Ni/Fe LDH and Ce-Ni/Fe LDH are consistent with the standard PDF #26-1286. At the same time, the characteristic peaks at 11.8°, 23.1°, 34.6°, and 60.3° correspond to the (003), (006), (012), and (110) planes of Ni/Fe LDH, respectively, proving the successful preparation of Ni/Fe LDH and Ce-Ni/Fe LDH. S@Ce-Ni/Fe LDH, obtained by melting and diffusion reactions with elemental sulfur, shows spiculate diffraction peaks of S₈, proving S₈ is in a good crystalline form in the material. The chemical composition and valence of Ce-Ni/Fe LDH were further studied by XPS, and the linear fitting was analyzed (Figure 3b–f). The spectrum in Figure 3b indicates the presence of the Ce, Ni, Fe, and O elements. As shown in Figure 3c, ten peaks are fitted for the Ce 3d high-resolution spectrum. Two binding energy peaks at 872.8 and 878.5 eV are

attributed to the $3d_{5/2}$ orbit of Ce^{3+} , and three binding energy peaks at 874.7, 880.2, and 882.7 eV are ascribed to the $3d_{5/2}$ orbit of Ce^{4+} . In addition, two peaks located at 893.6 and 900.4 eV are assigned to the $3d_{3/2}$ orbit of Ce^{3+} , and three binding energy peaks at 897, 903.9, and 909.8 eV are due to the $3d_{3/2}$ orbit of Ce^{4+} [26,27]. The Fe 2p high-resolution spectrum is presented in Figure 3d. The peaks at 707.3 eV and 721.5 eV are ascribed to the $2p_{3/2}$ orbit and $2p_{1/2}$ orbit of Fe^{2+} , and the peaks at 712.8 eV and 724.9 eV are assigned to the $2p_{3/2}$ orbit and $2p_{1/2}$ orbit of Fe^{3+} [28]. The peak at 718.5 eV is attributed to a satellite peak. It is seen from the above valence analysis of the Fe 2p high-resolution spectrum that Fe in the composite exists in the form of Fe^{3+} . Figure 3e shows the Ni 2p high-resolution spectrum. The two peaks at 855.5 and 873.1 eV are Ni $2p_{3/2}$ and Ni $2p_{1/2}$, respectively [29], which mainly exist in the form of Ni^{2+} . The two peaks at 861.9 and 879.7 eV are attributed to satellite peaks. Based on the valence analysis of the Fe 2p and Ni 2p high-resolution spectra, they are consistent with the existent forms of Ni and Fe in layered bimetallic hydroxide. Figure 3f displays the high-resolution spectrum of O 1s. The three binding energy peaks at 532.9, 531.0, and 529.7 eV belong to a metal–oxygen bond, hydroxide, and oxygen atoms attached to the material surface, respectively [30]. Most of them exist in the form of hydroxide. Combined with the analysis of the Ce 3d, Ni 2p, Fe 2p, and O 1s high-resolution spectra, the successful preparation of Ce-Ni/Fe LDH has been further demonstrated. The molar ratio of the Ni, Fe, and Ce ions in the Ce-Ni/Fe LDH composite is 3.5:1:0.15.

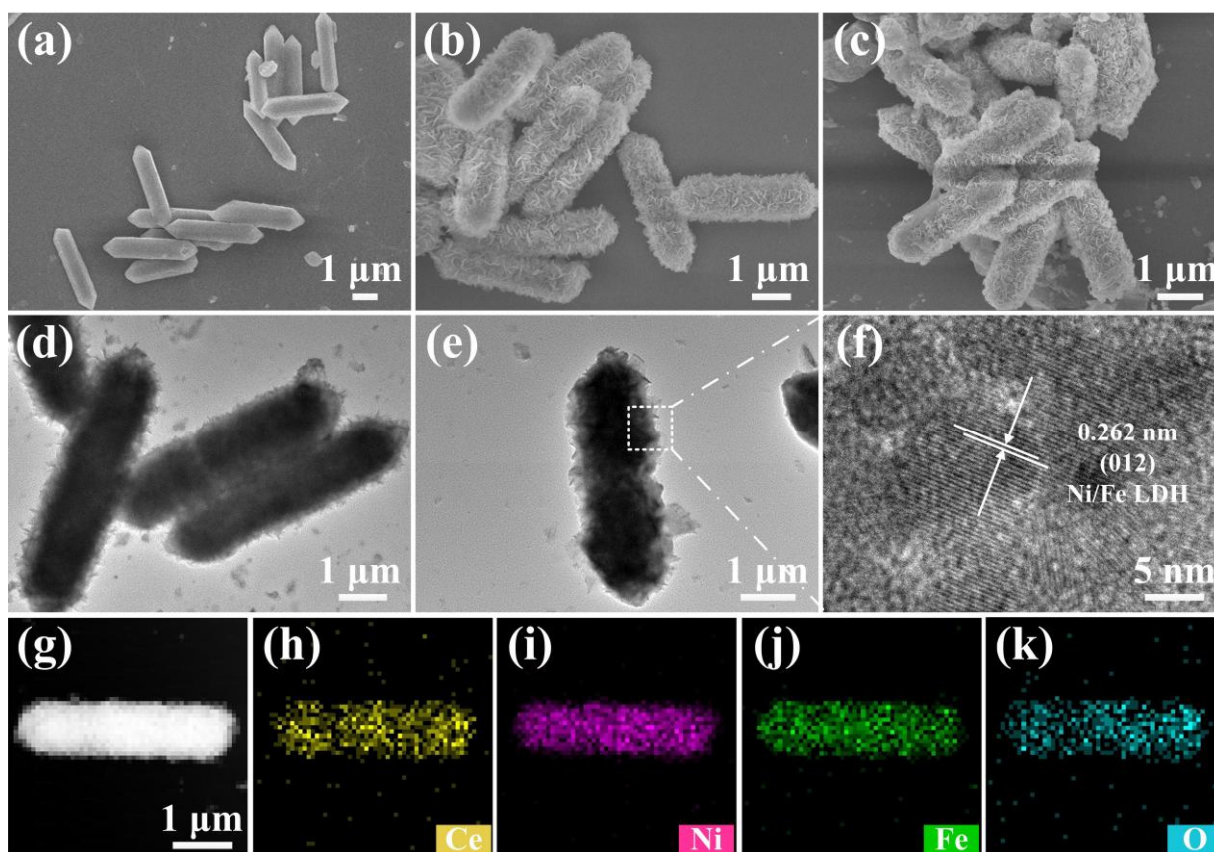


Figure 2. FESEM images of (a) the MIL-88A precursor, (b) Ce-Ni/Fe LDH, and (c) S@Ce-Ni/Fe LDH. (d,e) TEM and (f) HRTEM images of Ce-Ni/Fe LDH. (g) STEM image of Ce-Ni/Fe LDH, and (h–k) the corresponding elemental mappings of Ce, Ni, Fe, and O.

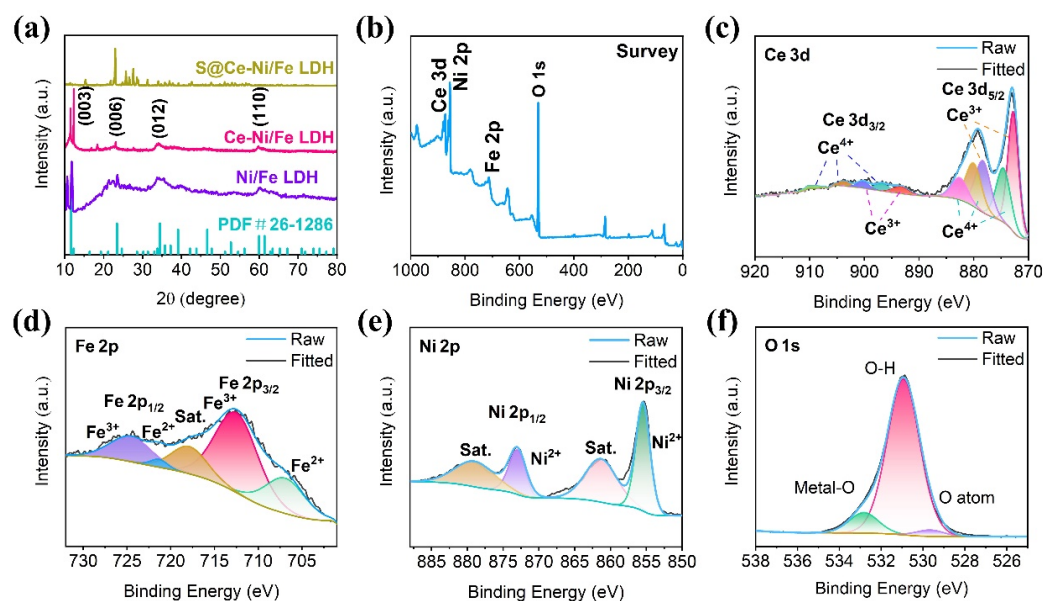


Figure 3. (a) XRD patterns of Ni/Fe LDH, Ce-Ni/Fe LDH, and S@Ce-Ni/Fe LDH. (b) XPS survey spectrum of Ce-Ni/Fe LDH. High-resolution XPS spectra of (c) Ce 3d, (d) Fe 2p, (e) Ni 2p, and (f) O 1s of Ce-Ni/Fe LDH.

To test the adsorption capacity of Ce-Ni/Fe LDH for LiPSs, we add Ce-Ni/Fe LDH and Ni/Fe LDH to the as-prepared Li_2S_6 solutions. As shown in the digital photos in Figure 4a, after 3 h, we observe that the color of the Ni/Fe LDH- Li_2S_6 solution changes from yellow to light yellow, while the Ce-Ni/Fe LDH- Li_2S_6 solution becomes almost clear and transparent. Therefore, Ce-Ni/Fe LDH has a better adsorption capacity for Li_2S_6 than Ni/Fe LDH. Additionally, the UV-Vis spectra are measured before and after the addition of Ce-Ni/Fe LDH and Ni/Fe LDH. Compared with the characteristic peak of the pure Li_2S_6 solution, the intensity of the absorption peak of the Ce-Ni/Fe LDH- Li_2S_6 solution is reduced significantly, and the abundant metal sites and groups in Ce-Ni/Fe LDH absorb LiPSs through the chemical action, indicating an inhibition effect on the dissolution and diffusion of LiPSs. Figure S5 shows the Ce 3d high-resolution XPS spectra of Ce-Ni/Fe LDH and Ce-Ni/Fe LDH- Li_2S_6 . After interacting with Li_2S_6 , the peaks of Ce^{3+} display low binding energies, showing the intense chemical interaction between Ce^{3+} and Li_2S_6 . In Figure S6, the wettability of pure S, S@Ni/Fe LDH, and S@Ce-Ni/Fe LDH electrode sheets to the electrolyte of a lithium-sulfur battery is compared. The wetting angles of pristine S, S@Ni/Fe LDH, and S@Ce-Ni/Fe LDH are 32.2° , 8.5° , and 6.4° , respectively. It is obvious that S@Ce-Ni/Fe LDH possesses the best wetting property and the strongest affinity for the electrolyte. The pore size distribution and specific surface area of Ce-Ni/Fe LDH are studied by the N_2 adsorption/desorption isothermal curve, and the results are shown in Figure 4b. The specific surface area of Ce-Ni/Fe LDH is $26.192 \text{ m}^2 \text{ g}^{-1}$, and mesopores account for the vast majority. The effective mesoporous materials expose more active surfaces and afford more sites for the adsorption of LiPSs [31–33]. The pore structure existing on the surface of Ce-Ni/Fe LDH can make the sulfur element enter better the laminate shell gap and the inside of the material. Meanwhile, the electrolyte will be easier to infiltrate and contact better with the active material, providing an effective path for ion transmission during cycling, so that the active material in the positive electrode material can be better utilized. The sulfur loading in S@Ce-Ni/Fe LDH is estimated by TGA under a nitrogen atmosphere. In Figure 4c, the mass loss is about 70 wt% below 350°C . Ce-Ni/Fe LDH remains stable under nitrogen protection; therefore, the mass loading of sulfur is about 70 wt% in S@Ce-Ni/Fe LDH. Figure 4d intuitively displays the inhibition of the shuttling effect by S@Ce-Ni/Fe LDH in a lithium-sulfur battery compared to the shuttling effect in a lithium-sulfur battery with pure sulfur.

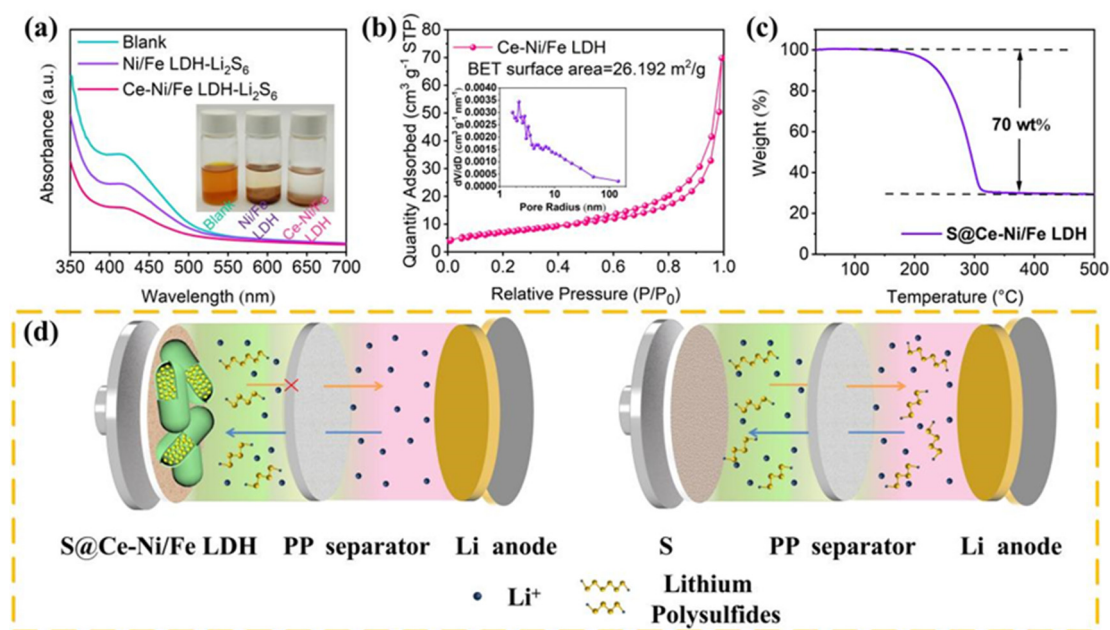


Figure 4. (a) UV–Vis spectra and digital photos of pure Li₂S₆ and Li₂S₆ solutions after adding Ni/Fe LDH and Ce-Ni/Fe LDH. (b) N₂ adsorption/desorption isotherm, and the pore size analysis (inset) of Ce-Ni/Fe LDH. (c) TGA curve of S@Ce-Ni/Fe LDH. (d) Schematic diagram of the suppression of the shuttling effect in a lithium–sulfur battery with S@Ce-Ni/Fe LDH, and a schematic diagram of the shuttling effect in a lithium–sulfur battery with pure sulfur.

To study the electrochemical performance of LSBs, we use different cathodes (S@Ce-Ni/Fe LDH, S@Ni/Fe LDH, and pure S) to assemble and test CR2025 button-type batteries, and the results are presented in Figure 5. Figure 5a displays the initial three CV curves of a lithium–sulfur battery with S@Ce-Ni/Fe LDH at 0.1 mV s⁻¹. There are two significant reduction peaks at 2.31 and 2.03 V, ascribed to the solid–liquid–solid transformation of S₈ → Li₂S_n (4 < n < 8) and Li₂S_n (4 < n < 8) → Li₂S₂/Li₂S, respectively. In addition, the oxidation peaks at 2.34 and 2.44 V are ascribed to the oxidation of Li₂S/Li₂S₂ with a short chain to Li₂S_n (4 < n < 8) with a long chain and the eventual oxidation to S₈, respectively [34–36]. Figure S7 indicates the above redox reaction mechanism of a lithium–sulfur battery with S@Ce-Ni/Fe LDH. It is found that the first three CV curves are highly coincident, ensuring that the redox reaction of a lithium–sulfur battery has good reversibility during charging/discharging processes [37–39]. Figure 5b shows the charging/discharging curves (1.7–2.8 V) of a lithium–sulfur battery using S@Ce-Ni/Fe LDH as the positive electrode material at different current densities. Fortunately, even with a current density up to 2 C, a lithium–sulfur battery with S@Ce-Ni/Fe LDH still maintains its well-defined plateaus [3,40–42], which is in keeping with the CV results (Figure 5a), ensuring the stable operation of the battery under a high current density. Figure S8 represents the charging/discharging curves of LSBs with S@Ni/Fe LDH and pure S at different current densities. It is obvious that the reversible capacities of LSBs with S@Ni/Fe LDH and pure S are lower than those of a lithium–sulfur battery with S@Ce-Ni/Fe LDH at the same current densities. Especially, as for a lithium–sulfur battery with pure S, there are no discharge plateaus at 0.3, 0.5, and 1 C, respectively. Figure S9a displays the initial charge/discharge curves of LSBs with S@Ce-Ni/Fe LDH, S@Ni/Fe LDH, and pure S at a current density of 0.1 C. The voltage gap (ΔE) between the charge platform and discharge plateau is derived from voltage hysteresis. Compared with LSBs with S@Ni/Fe LDH and pure sulfur, the ΔE value of the lithium–sulfur battery with S@Ce-Ni/Fe LDH is the smallest, indicating the improved redox kinetics. The bar chart in Figure S9b illustrates this gap more intuitively. As displayed in Figure 5c, we test the cycle performances of LSBs with S@Ce-Ni/Fe LDH, S@Ni/Fe LDH, and pure S at 0.2 C. The lithium–sulfur battery using S@Ce-Ni/Fe LDH

as the cathode material has a first discharge capacity of 1056 mAh g^{-1} . The discharge capacity is 759 mAh g^{-1} through 100 cycles, which is better than those of S@Ni/Fe LDH (419 mAh g^{-1}) and pure S (300 mAh g^{-1}), and the charge/discharge plateaus are still intact (Figure S10). The above results are comparable to the previously reported literatures (Table S2). Based on the calculations at the beginning of the second cycle, the capacity retention rate reaches a respectable 95%, strongly proving that S@Ce-Ni/Fe LDH inhibits the LiPSs produced during the cycling and increases the utilization rate of the active material. Figure S11 demonstrates two peaks in the negative part and two peaks in the positive part, which are consistent with the CV results in Figure 5a.

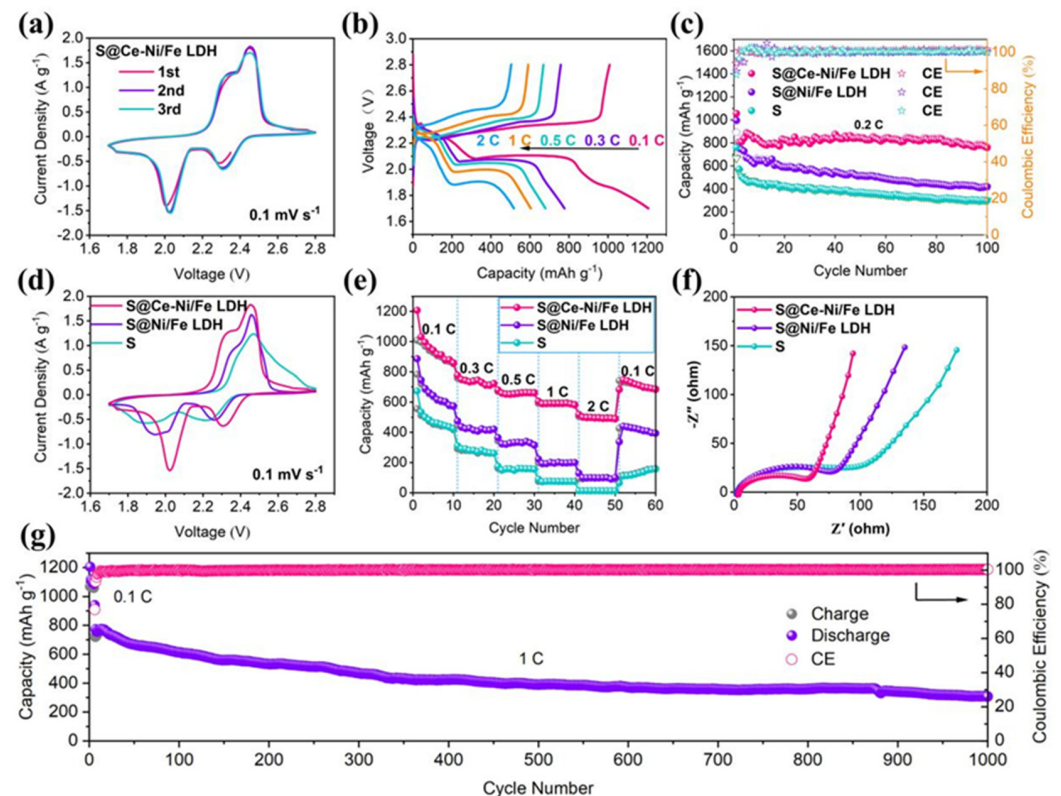


Figure 5. (a) CV curves of the lithium–sulfur battery with S@Ce-Ni/Fe LDH during the initial three cycles at 0.1 mV s^{-1} . (b) Charge/discharge curves of the lithium–sulfur battery with S@Ce-Ni/Fe LDH at different current densities. (c) Cycling performance and CE of the LSBs with S@Ce-Ni/Fe LDH, S@Ni/Fe LDH, and pure S for 100 cycles at 0.2 C. (d) CV curves at 0.1 mV s^{-1} , and (e) the rate performances of the LSBs with S@Ce-Ni/Fe LDH, S@Ni/Fe LDH, and pure S. (f) EIS spectra of the LSBs with S@Ce-Ni/Fe LDH, S@Ni/Fe LDH, and pure S before cycling. (g) Long-term cycling stability and CE of the lithium–sulfur battery with S@Ce-Ni/Fe LDH for 1000 cycles at 1 C.

At the scan rate of 0.1 mV s^{-1} , Figure 5d compares the CV results of the LSBs with S@Ce-Ni/Fe LDH, S@Ni/Fe LDH, and pure S. It is observed that the lithium–sulfur battery with S@Ce-Ni/Fe LDH has the sharpest reduction/oxidation peaks, and the distance between the reduction peak and oxidation peak is the smallest; that is, the polarization voltage is the lowest, indicating that it has the best redox kinetics [43–45]. As presented in Figure 5e, the rate performances of the LSBs with S@Ce-Ni/Fe LDH, S@Ni/Fe LDH, and pure S are tested. During the 0.1–2 C switching process, the lithium–sulfur battery with S@Ce-Ni/Fe LDH possesses the highest specific capacity, and the initial discharge capacity reaches 1207 mAh g^{-1} at 0.1 C. After the conversion process of different current densities and 60 cycles (returning to 0.1 C), it still maintains the discharge capacity of 690 mAh g^{-1} . Even at the high current density of 2 C, the lithium–sulfur battery with S@Ce-Ni/Fe LDH has still a discharge capacity of 489 mAh g^{-1} . However, the discharge capacities in the LSBs with pure S and S@Ni/Fe LDH decrease rapidly when switching to the higher current

density, which demonstrates that the polarization is serious under the high current density, fully indicating that the lithium–sulfur battery with S@Ce-Ni/Fe LDH possesses the best rate performance. The EIS spectra of the LSBs with S@Ce-Ni/Fe LDH, S@Ni/Fe LDH, and pure S are analyzed in Figure 5f. Each curve is made up of a semicircle and a slanted straight line, which are attributed to the charge transfer resistance (R_{ct}) derived from the diffusion of Li^+ and Warburg impedance (Z_w), respectively [46,47], as shown in an equivalent circuit diagram in Figure S12a. In the equivalent circuit diagram, R_e is the resistance of the electrolyte, and CPE stands for the interfacial capacitance [48]. The fitting of the EIS spectra of the LSBs with S@Ce-Ni/Fe LDH, S@Ni/Fe LDH, and pure S before cycling is shown in Figure S12b. According to the fitting results, among the three LSBs, the lithium–sulfur battery with S@Ce-Ni/Fe LDH has the lowest R_{ct} value (56 Ω), which is significantly lower than those of S@Ni/Fe LDH (75 Ω) and pure S (90 Ω). In addition, compared with the LSBs with S@Ni/Fe LDH and pure S, the lithium–sulfur battery with S@Ce-Ni/Fe LDH has the highest slope in the low-frequency region, demonstrating its fastest diffusion rate of Li^+ [49,50]. As shown in Figure 5g, the lithium–sulfur battery with S@Ce-Ni/Fe LDH is tested at 1 C for 1000 cycles. The battery is first activated at 0.1 C for five cycles, and then, the current density is returned to 1 C. The first specific capacity still remains at 940 mAh g^{-1} . After 1000 cycles, the specific capacity is kept at 308 mAh g^{-1} , and the average capacity attenuation rate per cycle is 0.067% (based on the second cycling). Figure S13 presents a digital photo of a light-emitting diode (LED) green lamp string lit up by two CR2025-type LSBs with S@Ce-Ni/Fe LDH connected in a series, fully showing the practical application prospect of this work for high-performance LSBs.

4. Conclusions

We successfully designed and prepared a capsule-type S@Ce-Ni/Fe LDH as a cathode material for LSBs, in which the 3D hollow Ce-Ni/Fe LDH is derived from the MIL-88A polyhedron. The unique capsule-like structure of Ce-Ni/Fe LDH possesses enough space to hold sulfur and a large amount of exposed active sites, which play an important role in preventing the dissolution and diffusion of LiPSs. Compared to the lithium–sulfur battery with the traditional sulfur cathode, the electrochemical properties of the lithium–sulfur battery with S@Ce-Ni/Fe LDH were significantly improved. The first discharge capacities of the lithium–sulfur battery with S@Ce-Ni/Fe LDH were 1207 and 1056 mAh g^{-1} at 0.1 and 0.2 C, respectively. Even at a large current density of 1 C, the lithium–sulfur battery with S@Ce-Ni/Fe LDH also delivered an initial discharge capacity of 940 mAh g^{-1} and could cycle 1000 times, with an average capacity decay rate per cycle of 0.067% (based on the second cycle). This work provided a new and simple idea to design a novel cathode carrier for high-performance LSBs. At the same time, the obtained active material supplies a direction for the development of other energy storage fields, such as room temperature Na-S batteries.

Supplementary Materials: The following supporting information can be downloaded at: <https://www.mdpi.com/article/10.3390/nano13152244/s1>, Figure S1: (a,b) FESEM images and (c) XRD pattern of MIL-88A precursor; Figure S2: (a,b) FESEM images of Ce-Ni/Fe LDH. (c,d) TEM images of Ce-Ni/Fe LDH; Figure S3: (a) SEM image and (b–e) corresponding elemental mappings of Ni/Fe LDH; Figure S4: (a) STEM image and (b–f) corresponding elemental mappings of S@Ce-Ni/Fe LDH; Figure S5: Ce 3d high-resolution XPS spectra of Ce-NiFe LDH and Ce-NiFe LDH-Li₂S₆; Figure S6: Contact angles between electrolyte and (a) pure S or (b) S@Ni/Fe LDH or (c) S@Ce-Ni/Fe LDH; Figure S7: Schematic illustration of the redox reaction mechanism of lithium-sulfur battery with S@Ce-Ni/Fe LDH; Figure S8: Charge/discharge curves of LSBs with (a) S@Ni/Fe LDH and (b) pure S at different current densities; Figure S9: (a) The first charge/discharge curves and (b) polarization voltage histograms of LSBs with S@Ce-Ni/Fe LDH, S@Ni/Fe LDH, and pure S at 0.1 C; Figure S10: The 100th charge/discharge curves of lithium-sulfur battery with S@Ce-Ni/Fe LDH at 0.2 C; Figure S11: dQ/dV plot of lithium-sulfur battery with S@Ce-Ni/Fe LDH at 0.2 C during the 100th cycle; Figure S12: (a) The equivalent circuit diagram of LSBs with S@Ce-Ni/Fe LDH, S@Ni/Fe LDH, and pure S before cycling. (b) The fitting of EIS spectra of LSBs with S@Ce-Ni/Fe LDH, S@Ni/Fe LDH, and pure S before cycling; Figure S13: Digital photo of a

light-emitting diode (LED) green lamp string lit up by two CR2025-type LSBs with S@Ce-Ni/Fe LDH connected in series; Table S1: Comparison of lithium-sulfur batteries with other major battery types; Table S2: Comparison of electrochemical performance of lithium-sulfur battery with S@Ce-Ni/Fe LDH with previously reported literatures. (References [51,52] are cited in the Supplementary Materials).

Author Contributions: Conceptualization, H.W. and Q.L.; methodology, B.J.; validation, H.W. and Q.L.; investigation, H.L. and B.J.; resources, B.J.; writing—original draft preparation, H.W. and Q.L.; writing—review and editing, H.L. and B.J.; supervision, B.J.; project administration, B.J.; and funding acquisition, B.J. All authors have read and agreed to the published version of the manuscript.

Funding: This work was funded by the National Natural Science Foundation of China (No. 52130101) and the Project of Science and Technology Development Plan of Jilin Province in China (Nos. 20210402058GH and 20220201114GX).

Institutional Review Board Statement: Not applicable.

Informed Consent Statement: Not applicable.

Data Availability Statement: Not available.

Conflicts of Interest: The authors declare no conflict of interest.

References

1. Cao, X.-H.; Tan, C.-L.; Sindoro, M.; Zhang, H. Hybrid Micro-/Nano-Structures Derived From Metal-Organic Frameworks: Preparation and Applications in Energy Storage and Conversion. *Chem. Soc. Rev.* **2017**, *46*, 2660–2677. [[CrossRef](#)] [[PubMed](#)]
2. Manthiram, A.; Fu, Y.-Z.; Chung, S.-H.; Zu, C.-X.; Su, Y.-S. Rechargeable Lithium-Sulfur Batteries. *Chem. Rev.* **2014**, *114*, 11751–11787. [[CrossRef](#)] [[PubMed](#)]
3. Wu, H.-L.; Li, Y.; Ren, J.; Rao, D.-W.; Zheng, Q.-J.; Zhou, L.; Lin, D. CNT-Assembled Dodecahedra Hydroxide Nanosheet Shell Enabled Sulfur Cathode for High-Performance Lithium-Sulfur Batteries. *Nano Energy* **2018**, *55*, 82–92. [[CrossRef](#)]
4. Bao, W.-Z.; Liu, L.; Wang, C.-Y.; Choi, S.-H.; Wang, D.; Wang, G.-X. Facile Synthesis of Crumpled Nitrogen-Doped MXene Nanosheets as a New Sulfur Host for Lithium-Sulfur Batteries. *Adv. Energy Mater.* **2017**, *8*, 1702485. [[CrossRef](#)]
5. Liu, X.; Huang, J.-Q.; Zhang, Q.; Mai, L.-Q. Nanostructured Metal Oxides and Sulfides for Lithium-Sulfur Batteries. *Adv. Mater.* **2017**, *29*, 1601759. [[CrossRef](#)]
6. Fan, Q.; Liu, W.; Wen, Z.; Sun, Y.-M.; Wang, H.-L. Ternary Hybrid Material for High-Performance Lithium-Sulfur Battery. *J. Am. Chem. Soc.* **2015**, *137*, 12946–12953. [[CrossRef](#)]
7. Lin, H.-B.; Zhang, S.-L.; Zhang, T.-R.; Ye, H.-L.; Yao, Q.-F.; Zheng, G.-Y.; Lee, J.Y. Simultaneous Cobalt and Phosphorous Doping of MoS₂ for Improved Catalytic Performance on Polysulfide Conversion in Lithium-Sulfur Batteries. *Adv. Energy Mater.* **2019**, *9*, 1902096. [[CrossRef](#)]
8. Chen, T.; Ma, L.-B.; Cheng, B.-R.; Chen, R.-P.; Hu, Y.; Zhu, G.-Y.; Wang, Y.-R.; Liang, J.; Tie, Z.-X.; Liu, J.; et al. Metallic and Polar Co₉S₈ Inlaid Carbon Hollow Nanopolyhedra as Efficient Polysulfide Mediator for Lithium-Sulfur Batteries. *Nano Energy* **2017**, *38*, 239–248. [[CrossRef](#)]
9. Li, Q.-C.; Liu, H.; Jin, B.; Li, L.; Sheng, Q.-D.; Cui, M.-Y.; Li, Y.-Y.; Lang, X.-Y.; Zhu, Y.-F.; Zhao, L.-J.; et al. Anchoring Polysulfides via a CoS₂/NC@1T MoS₂ Modified Separator for High-Performance Lithium-Sulfur Batteries. *Inorg. Chem. Front.* **2023**, *10*, 959–971. [[CrossRef](#)]
10. Sun, W.-W.; Liu, C.; Li, Y.-J.; Luo, S.-Q.; Liu, S.-K.; Hong, X.-B.; Xie, K.; Liu, Y.M.; Tan, X.-J.; Zheng, C.-M. Rational Construction of Fe₂N@C Yolk-Shell Nanoboxes as Multifunctional Hosts for Ultralong Lithium-Sulfur Batteries. *ACS Nano* **2019**, *13*, 12137–12147. [[CrossRef](#)]
11. Cao, Z.-X.; Jia, J.-Y.; Chen, S.-N.; Li, H.-H.; Sang, M.; Yang, M.-G.; Wang, X.-X.; Yang, S.-T. Integrating Polar and Conductive Fe₂O₃-Fe₃C Interface with Rapid Polysulfide Diffusion and Conversion for High-Performance Lithium-Sulfur Batteries. *ACS Appl. Mater. Interfaces* **2019**, *11*, 39772–39781. [[CrossRef](#)]
12. Zhou, H.-Y.; Sui, Z.-Y.; Amin, K.; Lin, L.-Y.; Wang, H.-Y.; Han, B.-H. Investigating the Electrocatalysis of a Ti₃C₂/Carbon Hybrid in Polysulfide Conversion of Lithium-Sulfur Batteries. *ACS Appl. Mater. Interfaces* **2020**, *12*, 13904–13913. [[CrossRef](#)]
13. Xiao, D.-J.; Li, Q.; Zhang, H.-F.; Ma, Y.-Y.; Lu, C.-X.; Chen, C.-M.; Liu, Y.-D.; Yuan, S.-X. A Sulfur Host Based on Cobalt-Graphitic Carbon Nanocages for High Performance Lithium-Sulfur Batteries. *J. Mater. Chem. A* **2017**, *5*, 24901. [[CrossRef](#)]
14. Zhang, J.-T.; Li, Z.; Chen, Y.; Gao, S.-Y.; Lou, X.-W. Nickel-Iron Layered Double Hydroxide Hollow Polyhedrons as a Superior Sulfur Host for Lithium-Sulfur Batteries. *Angew. Chem. Int. Ed.* **2018**, *57*, 10773–11077.
15. Hwang, J.-Y.; Kim, H.-M.; Shin, S.-B.; Sun, Y.-K. Designing a High-Performance Lithium-Sulfur Batteries Based on Layered Double Hydroxides-Carbon Nanotubes Composite Cathode and a Dual-Functional Graphene-Polypropylene-Al₂O₃ Separator. *Adv. Funct. Mater.* **2018**, *28*, 1704294. [[CrossRef](#)]
16. Chen, S.-X.; Luo, J.-H.; Li, N.-Y.; Han, X.-X.; Wang, J.; Deng, Q.; Zeng, Z.-L.; Deng, S.-G. Multifunctional LDH/Co₉S₈ Heterostructure Nanocages as High-Performance Lithium-Sulfur Battery Cathodes with Ultralong Lifespan. *Energy Storage Mater.* **2020**, *30*, 187–195. [[CrossRef](#)]

17. Zhang, J.-T.; Hu, H.; Li, Z.; Lou, X.-W. Double-Shelled Nanocages with Cobalt Hydroxide Inner Shell and Layered Double Hydroxides Outer Shell as High-Efficiency Polysulfide Mediator for Lithium-Sulfur Batteries. *Angew. Chem. Int. Ed.* **2016**, *55*, 3982–3986. [[CrossRef](#)]
18. Poudel, M.B.; Kim, A.A.; Lohani, P.C.; Yoo, D.J.; Kim, H.J. Assembling Zinc Cobalt Hydroxide/Ternary Sulfides Heterostructure and Iron Oxide Nanorods on Three-dimensional Hollow Porous Carbon Nanofiber as High Energy Density Hybrid Supercapacitor. *J. Energy Storage* **2023**, *60*, 106713. [[CrossRef](#)]
19. Poudel, M.B.; Lohani, P.C.; Acharya, D.; Kande, D.R.; Kim, A.A.; Yoo, D.J. MOF Derived Hierarchical ZnNiCo-LDH on Vapor Solid Phase Grown Cu_xO Nanowire Array as High Energy Density Asymmetric Supercapacitors. *J. Energy Storage* **2023**, *72*, 108220. [[CrossRef](#)]
20. Poudel, M.B.; Shin, M.; Kim, H.J. Interface Engineering of MIL-88 Derived MnFe-LDH and MnFe₂O₃ on Three-dimensional Carbon Nanofibers for the Efficient Adsorption of Cr(VI), Pb(II), and As(III) Ions. *Sep. Purif. Technol.* **2022**, *287*, 120463. [[CrossRef](#)]
21. Xu, H.-J.; Shan, C.-F.; Wu, X.-X.; Sun, M.-Z.; Huang, B.-L.; Tang, Y.; Yan, C.-H. Fabrication of Layered Double Hydroxide Microcapsules Mediated by Cerium Doping in Metal-Organic Frameworks for Boosting Water Splitting. *Energy Environ. Sci.* **2020**, *13*, 2949. [[CrossRef](#)]
22. Baumann, A.E.; Aversa, G.E.; Roy, A.; Falk, M.L.; Bedford, N.M.; Thoi, V.S. Promoting Sulfur Adsorption Using Surface Cu Sites in Metal-Organic Frameworks for Lithium Sulfur Batteries. *J. Mater. Chem. A* **2018**, *6*, 4811–4821. [[CrossRef](#)]
23. Xu, F.-C.; Dong, C.-W.; Jin, B.; Li, H.; Wen, Z.; Jiang, Q. MOF-Derived LDH Wrapped with rGO as an Efficient Sulfur Host for Lithium-Sulfur Batteries. *J. Electroanal. Chem.* **2020**, *876*, 114545. [[CrossRef](#)]
24. Mou, J.-R.; Li, Y.-J.; Ou, L.-Q.; Huang, J.-L. A Highly-Efficient Electrocatalyst for Room Temperature Sodium-Sulfur Batteries: Assembled Nitrogen-Doped Hollow Porous Carbon Spheres Decorated with Ultrafine α -MoC_{1-x} Nanoparticles. *Energy Storage Mater.* **2022**, *52*, 111–119. [[CrossRef](#)]
25. Zhou, W.; Zhao, D.-K.; Wu, Q.-K.; Fan, B.; Zhu, X.-J.; Dan, J.-C.; Li, N.-W.; Lei, W.; Li, L.-G. Enhancing the Adsorption and Catalytic Conversion of Polysulfides by Nitrogen Doped Carbon Micro-Flowers Embedded with Mo₂C Nanoparticles. *Carbon* **2021**, *178*, 371–381. [[CrossRef](#)]
26. Zhao, H.-P.; Du, X.-Q.; Zhang, X.-S. Interfacing or Doping? Role of Ce in Water Oxidation Reaction and Urea Oxidation Reaction of N-Ni₃S₂. *J. Alloys Compd.* **2022**, *925*, 166662. [[CrossRef](#)]
27. Liu, M.-J.; Min, K.-A.; Han, B.-C.; Lee, L.Y.S. Interfacing or Doping? Role of Ce in Highly Promoted Water Oxidation of NiFe-Layered Double Hydroxide. *Adv. Energy Mater.* **2021**, *11*, 2101281. [[CrossRef](#)]
28. Mohammed, A.-T.; Dong, Y.-T.; Zhang, R.; Zhang, Y.-Y.; Zhang, J.-M. Understanding the High-Performance Fe(OH)₃@GO Nanoarchitecture as Effective Sulfur Hosts for the High Capacity of Lithium-Sulfur Batteries. *Appl. Surf. Sci.* **2021**, *538*, 148032.
29. Wen, C.-Y.; Zheng, X.-Z.; Li, X.-Y.; Yuan, M.-W.; Li, H.-F.; Sun, G.-B. Rational Design of 3D Hierarchical MXene@AlF₃/Ni(OH)₂ Nanohybrid for High-Performance Lithium-Sulfur Batteries. *Chem. Eng. J.* **2021**, *409*, 128102. [[CrossRef](#)]
30. Zhu, W.-J.; Chen, W.-X.; Yu, H.-H.; Zeng, Y.; Ming, F.-W.; Liang, H.-F.; Wang, Z.C. NiCo/NiCo-OH and NiFe/NiFe-OH Core Shell Nanostructures for Water Splitting Electrocatalysis at Large Currents. *Appl. Catal. B Environ.* **2020**, *278*, 119326. [[CrossRef](#)]
31. Chang, Y.-G.; Ren, Y.-M.; Zhu, L.-K.; Li, Y.; Li, T.; Ren, B.-Z. Preparation of Macadamia Nut Shell Porous Carbon and its Electrochemical Performance as Cathode Material for Lithium-Sulfur Batteries. *Electrochim. Acta* **2022**, *420*, 140454. [[CrossRef](#)]
32. Ren, G.; Li, S.; Fan, Z.-X.; Warzywodac, J.; Fan, Z. Soybean-Derived Hierarchical Porous Carbon with Large Sulfur Loading and Sulfur Content for High-Performance Lithium-Sulfur Batteries. *J. Mater. Chem. A* **2016**, *4*, 16507–16515. [[CrossRef](#)]
33. Wang, N.-N.; Xu, Z.-F.; Xu, X.; Liao, T.; Tang, B.; Bai, Z.-C.; Dou, S.-X. Synergistically Enhanced Interfacial Interaction to Polysulfide via N,O Dual-Doped Highly Porous Carbon Microrods for Advanced Lithium-Sulfur Batteries. *ACS Appl. Mater. Interfaces* **2018**, *10*, 13573–13580. [[CrossRef](#)]
34. Li, H.-H.; Wang, Y.-X.; Chen, H.-Q.; Niu, B.-X.; Zhang, W.-C.; Wu, D.-P. Synergistic Mediation of Polysulfide Immobilization and Conversion by a Catalytic and Dual-Adsorptive System for High Performance Lithium-Sulfur Batteries. *Chem. Eng. J.* **2021**, *406*, 126802. [[CrossRef](#)]
35. Zhang, Y.-Z.; Ge, X.; Kang, Q.; Kong, Z.-K.; Wang, Y.-L.; Zhan, L. Vanadium Oxide Nanorods Embed in Porous Graphene Aerogel as High-Efficiency Polysulfide-Trapping-Conversion Mediator for High Performance Lithium-Sulfur Batteries. *Chem. Eng. J.* **2020**, *393*, 124570. [[CrossRef](#)]
36. Shen, J.-D.; Xu, X.-J.; Liu, J.; Liu, Z.-B.; Li, F.-K.; Hu, R.-Z.; Liu, J.-W.; Hou, X.H.; Feng, Y.-Z.; Yu, Y.; et al. Mechanistic Understanding of Metal Phosphide Host for Sulfur Cathode in High-Energy-Density Lithium-Sulfur Batteries. *ACS Nano* **2019**, *13*, 8986–8996. [[CrossRef](#)]
37. Fei, B.; Zhang, C.-Q.; Cai, D.-P.; Zheng, J.-Y.; Chen, Q.-D.; Xie, Y.-L.; Zhu, L.-Z.; Cabot, A.; Zhan, H.B. Hierarchical Nanoreactor with Multiple Adsorption and Catalytic Sites for Robust Lithium-Sulfur Batteries. *ACS Nano* **2021**, *15*, 6849–6860. [[CrossRef](#)]
38. Song, Z.-H.; Jiang, W.-Y.; Jian, X.-G.; Hu, F.-Y. Advanced Nanostructured Materials for Electrocatalysis in Lithium-Sulfur Batteries. *Nanomaterials* **2022**, *12*, 4341. [[CrossRef](#)]
39. Niu, S.-Q.; Hu, C.-C.; Liu, Y.-Y.; Zhao, Y.; Yin, F.-X. Nanoporous Co and N-Codoped Carbon Composite Derived from ZIF-67 for High-Performance Lithium-Sulfur Batteries. *Nanomaterials* **2021**, *11*, 1910. [[CrossRef](#)]
40. Li, Y.J.; Fang, J.M.; Zhang, J.H.; Yang, J.F.; Yuan, R.M.; Chang, J.K.; Zheng, M.S.; Dong, Q.F. A Honeycomb-like Co@N-C Composite for Ultrahigh Sulfur Loading Li-S Batteries. *ACS Nano* **2017**, *11*, 11417–11424. [[CrossRef](#)]

41. Ge, X.-L.; Li, C.-X.; Li, Z.-Q.; Yin, L.-W. Tannic Acid Tuned Metal-Organic Framework as a High-Efficiency Chemical Anchor of Polysulfide for Lithium-Sulfur Batteries. *Electrochim. Acta* **2018**, *281*, 700–709. [[CrossRef](#)]
42. Kang, X.; Bernardo, L.D.; Yang, H.-L.; Torres, J.F.; Zhang, L. Metal-Organic Framework Microdomains in 3D Conductive Host as Polysulfide Inhibitor for Fast, Long-Cycle Li-S Batteries. *Appl. Surf. Sci.* **2021**, *535*, 147680. [[CrossRef](#)]
43. Cui, G.-L.; Li, G.-R.; Luo, D.; Zhang, Y.-G.; Zhao, Y.; Wang, D.-R.; Wang, J.-Y.; Zhang, Z.; Wang, X.; Chen, Z.-W. Three-Dimensionally Ordered Macro-Microporous Metal Organic Frameworks with Strong Sulfur Immobilization and Catalyzation for High-Performance Lithium-Sulfur Batteries. *Nano Energy* **2020**, *72*, 104685. [[CrossRef](#)]
44. Wu, Z.-L.; Wang, L.; Chen, S.-X.; Zhu, X.-M.; Deng, Q.; Wang, J.; Zeng, Z.-L.; Deng, S.-G. Facile and Low-Temperature Strategy to Prepare Hollow ZIF-8/CNT Polyhedrons as High-Performance Lithium-Sulfur Cathodes. *Chem. Eng. J.* **2021**, *404*, 126579. [[CrossRef](#)]
45. Liang, X.; Garsuch, A.; Nazar, L.F. Sulfur Cathodes Based on Conductive MXene Nanosheets for High-Performance Lithium-Sulfur Batteries. *Angew. Chem.* **2015**, *54*, 3907–3911. [[CrossRef](#)]
46. Li, H.; Zhao, M.; Jin, B.; Wen, Z.; Liu, H.-K.; Jiang, Q. Mesoporous Nitrogen-Doped Carbon Nanospheres as Sulfur Matrix and a Novel Chelate-Modified Separator for High-Performance Room-Temperature Na-S Batteries. *Small* **2020**, *16*, 1907464. [[CrossRef](#)]
47. Li, H.; Zhou, Y.-T.; Zhao, M.; Jin, B.; Wen, Z.; Xie, H.-M.; Dou, S.-X.; Jiang, Q. Suppressed Shuttle via Inhibiting the Formation of Long-Chain Lithium Polysulfides and Functional Separator for Greatly Improved Lithium-Organosulfur Batteries Performance. *Adv. Energy Mater.* **2020**, *10*, 1902695. [[CrossRef](#)]
48. Liu, H.; Yang, X.-J.; Jin, B.; Cui, M.-Y.; Li, Y.-Y.; Li, Q.-C.; Li, L.; Sheng, Q.-D.; Lang, X.-Y.; Jin, E.-M.; et al. Coordinated Immobilization and Rapid Conversion of Polysulfide Enabled by a Hollow Metal Oxide/Sulfide/Nitrogen-Doped Carbon Heterostructure for Long-Cycle-Life Lithium-Sulfur Batteries. *Small* **2023**, 2300950. [[CrossRef](#)]
49. Han, G.-D.; Wang, X.; Yao, J.; Zhang, M.; Wang, J. The Application of Indium Oxide@CPM-5-C-600 Composite Material Derived from MOF in Cathode Material of Lithium Sulfur Batteries. *Nanomaterials* **2020**, *10*, 177. [[CrossRef](#)]
50. Xie, J.; Peng, H.-J.; Song, Y.-W.; Li, B.-Q.; Xiao, Y.; Zhao, M.; Yuan, H.; Huang, J.-Q.; Zhang, Q. Spatial and Kinetic Regulation of Sulfur Electrochemistry on Semi-Immobilized Redox Mediators in Working Batteries. *Angew. Chem. Int. Ed.* **2020**, *59*, 17670–17675. [[CrossRef](#)]
51. Wei, H.-J.; Liu, J.; Liu, Y.; Wang, L.; Li, L.-L.; Wang, F.; Ren, X.-Y.; Ren, F.-Z. Hollow Co-Fe LDH as an Effective Adsorption/Catalytic Bifunctional Sulfur Host For High-Performance Lithium-Sulfur Batteries. *Compos. Commun.* **2021**, *28*, 100973. [[CrossRef](#)]
52. Liu, Q.; Zhang, Y.-Q.; Zhou, Y.-B.; Wang, M.; Li, R.-L.; Yue, W.-B. Layered Double Hydroxides Used as the Sulfur Hosts for Lithium-Sulfur Batteries and the Influence of Metal Composition on Their Performance. *J. Solid State Electr.* **2023**, *27*, 797–807. [[CrossRef](#)]

Disclaimer/Publisher's Note: The statements, opinions and data contained in all publications are solely those of the individual author(s) and contributor(s) and not of MDPI and/or the editor(s). MDPI and/or the editor(s) disclaim responsibility for any injury to people or property resulting from any ideas, methods, instructions or products referred to in the content.